Biosensors and Bioelectronics 136 (2019) 53–59

Contents lists available at ScienceDirect

Biosensors and Bioelectronics

journal homepage: www.elsevier.com/locate/bios

All-electrodeposited amorphous MoS_x@ZnO core-shell nanorod arrays for self-powered visible-light-activated photoelectrochemical tobramycin aptasensing

Mengxiang Shang[a], Jinling Zhang[a], Hui Qi[b], Yao Gao[a], Jianyue Yan[a], Wenbo Song[a,*]

[a] College of Chemistry, Jilin University, Changchun, 130012, PR China
[b] The Second Hospital of Jilin University, Changchun, 130041, PR China

ARTICLE INFO

Keywords:
Amorphous molybdenum sulfide
ZnO nanorod arrays
All-electrochemical approach
Self-powered
Photoelectrochemical aptasensor
Tobramycin

ABSTRACT

The design and construction of high-performance photoelectrode with efficient visible-light absorption and fast charge transport rate are crucial to developing photoelectrochemical (PEC) sensor. Herein, a well-aligned amorphous MoS_x (a-MoS_x)@ZnO core-shell nanorod arrays was uniformly grown on indium tin oxide (ITO) via a facile all-electrochemical strategy. Simultaneous boosted PEC performance and stability in the visible region were obtained. Those could be attributed to the collaboration effect of fast electron transfer path within the oriented ZnO nanorod and extended visible-light absorption upon combining a-MoS_x, as well as favorable energy-band alignment between the two PEC materials. By employing tobramycin-binding aptamer as recognition element, a self-powered PEC aptasensor for tobramycin was successfully fabricated for the first time. The sensor exhibited a rapid response in a wide linear range of 0.010–50 ng/mL with good stability and reproducibility. The detection limit was as low as 5.7 pg/mL. Ultrasensitive and high-affinitive determination of tobramycin in serum samples was realized at 0 V (vs.SCE) with desired accuracy and satisfactory recovery. This work reveals the promising application of all-electrodeposited a-MoS_x@ZnO NR arrays-based photoanode for self-powered PEC bioassay in the tobramycin-related disease diagnosis.

1. Introduction

Tobramycin (TOB) is an aminoglycoside antibiotic that possesses bactericidal activity against a broad spectrum of bacteria, particularly pseudomonas aeruginosa (Guo et al., 2006). Incorrect and overdosed use of TOB could cause accumulation in human, leading to a risk for human health. The therapeutic range of TOB in serum is restricted in a range of 2–12 μg/mL due to serious irreversible side effects such as nephron-toxicity, neuromuscular blocking and hypersensitivity (Gonzalez-Fernandez et al., 2011; Gupta et al., 2013). Currently, various strategies have been involved to determinate TOB including high-performance liquid chromatography (Rosasco et al., 2018), transmission-localized surface plasmon resonance (Cappi et al., 2015), electrochemistry (Gonzalez-Fernandez et al., 2013; Wang et al., 2018), fluorescence spectroscopy (Han et al., 2018), and UV–Vis absorption spectroscopy (Ma et al., 2018). However, to precisely monitor the change of trace amount of TOB in complex biological matrices, simple and convenient new strategy with lower background signal and better stability is urgently desired. Possessing advantages of conventional electrochemical and optical methods along with high specificity of aptamer, photoelectrochemical (PEC) aptasensing exhibits high sensitivity and selectivity, fast response, low background noise and low cost (Tu et al., 2018; Zhao et al., 2016). Particularly, certain PEC aptasensors even can work under zero-bias, efficiently avoiding the interference of other biomolecules (Arechederra and Minteer, 2011; Peng et al., 2018). These merits make PEC aptasensing to be a promising alternative for precise monitoring trace amount of TOB in biological systems.

In a typical PEC aptasenor, the photoactive material converts photoirradiation to electrical signal which has a dose-responsive relation with the analyte (Zang et al., 2018). Obviously, the photoactive material plays a key role in improving the sensitivity of the PEC aptasensor (Devadoss et al., 2015). Unfortunately, the prevalent photoactive materials (eg. TiO_2, ZnO, NiO) possess relatively wide band gap, which are far from satisfactory because of high charge carrier recombination rate and limited visible-light absorption (Gu et al., 2015; Jin et al., 2015; Yang et al., 2017). On the other hand, narrow bandgap semiconductors such as CdS, CdSe, CdTe and PbS are toxic to biomolecules and

* Corresponding author.
E-mail address: wbsong@jlu.edu.cn (W. Song).

https://doi.org/10.1016/j.bios.2019.04.019
Received 14 January 2019; Received in revised form 3 April 2019; Accepted 10 April 2019
Available online 23 April 2019
0956-5663/

environment, which restricts their practical application (Gong et al., 2018; Liu et al., 2017; Miao et al., 2013). Therefore, design and exploration of non-poisonous visible-light-sensitive photoactive materials are crucial for developing high-performance PEC aptasensor.

As a non-poisonous photoactive semiconductor with a narrow band gap, nanostructured molybdenum sulfide (MoS_x) emerges as an ideal candidate of visible-light sensitive photoactive materials for photocatalytic and PEC scopes. To date, much effort has been devoted to exploring crystalline MoS_2-based photoactive materials (Chen et al., 2013; Wu et al., 2017). These crystalline materials are normally prepared via hydrothermal reaction or high-temperature sulfurization reaction, which products are usually powder-type (Dunne et al., 2015; Huang et al., 2015). For obtaining a photoelectrode, the powder material should be loaded onto a conductive substrate by drop-casting or film-coating procedure (Du et al., 2015; Jiang et al., 2019). Such a photoelectrode might suffer from certain limitations including poor conductivity and stability and reproducibility. By contrast, amorphous MoS_x (a-MoS_x) prepared by electrodeposition can be directly grown on conduction substrate with strong adhesion, uniform coverage and good electrical continuity (Shang et al., 2018b). Moreover, recent advance demonstrates that a-MoS_x possesses stronger visible-light absorption and higher catalytic activity than crystalline MoS_x nanomaterials, attributed to unique structure feature (Benck et al., 2012; Morales-Guio and Hu, 2014). Besides, a-MoS_x is readily achieved by facile electrodeposition under mild conditions, which makes it more suitable as a low-cost photoelectrode for PEC application. However, the charge transfer in a-MoS_x is still limited by poor crystallinity, which hampers the photocurrent response. To overcome this drawback, construction of heterostructures between a-MoS_x and other semiconductors is suggested to be an efficient strategy (Liu et al., 2018; Tan et al., 2018). In this regard, ZnO nanorod (NR) is considered as an ideal material, owing to its large surface area, high carrier mobility, good chemical stability and nontoxicity (Kang et al., 2016; Li et al., 2018; Yang and Cheng, 2018). By coupling a-MoS_x and ZnO NR, the photogenerated electron-hole pairs could be effectively separated and transferred through direct electrical pathway in aligned one-dimensional nanorods. In addition, well-matched energy band alignment formed between a-MoS_x and ZnO NR might further promote separation/transport of the photogenerated charge carriers in the heterostructure, thereby generating high PEC activity. To date, study on a-MoS_x/ZnO NR heterostructure and its application as photoanode for PEC aptasensing have not been reported.

Herein, a visible-light-activated a-MoS_x@ZnO NR arrays has been fabricated by sequential electrodeposition, its application as high-performance photoelectrode for self-powered PEC aptasensor towards TOB in biological system has also been demonstrated for the first time. In this system, enhanced photocurrent in the visible region could be achieved due to the advantages of a-MoS_x@ZnO heterostructure, which may benefit for construction of high sensitive sensing interface. By immobilizing label-free aptamer as the biorecognition element, precise detection of trace amount of TOB in biological system could be realized. Additionally, the self-powered PEC sensor operating at zero bias voltage can effectively exclude the interferences from other reductive biomolecules in the detection system. The reliability of the proposed PEC sensor in TOB determination in real samples is also evaluated.

2. Experimental section

2.1. Electrochemical growth of ZnO NR arrays

The reagents and apparatus are shown in the Supplemental material. ZnO NR arrays was prepared by electrochemical deposition, according to previous reports with slight modifications (Lu et al., 2014; Miao et al., 2013). The electrodeposition was performed in a standard three-electrode configuration containing an ITO sheet working electrode, a saturated Ag/AgCl reference electrode, and a graphite rod counter electrode. Prior to electrodeposition, the ITO-coated glass sheet was cleaned with acetone, 0.1 M NaOH solution (ethanol: H_2O = 1:1; v/v) and ultrapure water under sonication for 15 min, respectively. Electrodeposition was performed by using a multi-potential step technique in a 5 mM $Zn(NO_3)_2$ aqueous solution containing 0.05 M $NaNO_3$ as a supporting electrolyte in 80 °C water bath. Briefly, the ITO sheet was firstly dipped into 0.1 mM KOH solution for 2 min and a ZnO seed-layer was then coated through electrodeposition at a potential of −1.3 V (vs. Ag/AgCl) for 10 s. Subsequently, a constant potential of 1.0 V (vs. Ag/AgCl) was applied for 900 s. The ITO/ZnO NR arrays electrode was thoroughly rinsed with ultrapure water and dried at 80 °C, followed by annealing at 350 °C in air for 10 min. To obtain the well oriented ZnO NR arrays, the deposition conditions including deposition time, deposition temperature and $Zn(NO_3)_2$ concentration were optimized (Fig. S1).

2.2. Fabrication of a-MoS_x@ZnO NR arrays

Similar to that in our previous report (Shang et al., 2018a), the electrodeposition of a-MoS_x thin film was carried out in a regular three-electrode system with an ITO/ZnO (or bare ITO) as the working electrode, a SCE and Pt plate as the reference and counter electrodes, at a constant potential of 1.4 V (vs. SCE) for 100 s in a 2 mM $(NH_4)_2MoS_4$ aqueous solution using 0.1 M $NaClO_4$ as the supporting electrolyte. The resultant ITO/a-MoS_x@ZnO NR arrays electrode (denoted as ITO/a-MoS_x@ZnO NR arrays) was thoroughly rinsed with ultrapure water and then dried under vacuum at 60 °C.

2.3. Construction of PEC aptasensor

The as-prepared ITO/a-MoS_x@ZnO NR arrays electrode was firstly coated with 20 μL of 0.3% chitosan solution in 0.1% (v/v) acetic acid aqueous solution. After drying at room temperature for 1 h, the electrode was rinsed with 10 mM PBS and dried in a nitrogen atmosphere. Subsequently, 20 μL of 50 nM TOB-targeted aptamer solution (containing 50 mM EDC) was casted onto the electrode surface. After incubating at 37 °C for 2 h, the electrode was thoroughly rinsed with 10 mM PBS to remove the unbounded aptamer. Facile immobilizing aptamer on the ITO/a-MoS_x@ZnO NR arrays electrode relied on the formation of phosphoramidate bonds between the amino group of chitosan and the phosphate group of aptamer (Bo et al., 2011; Liu et al., 2012). The resulting aptasensor was denoted briefly as ITO/a-MoS_x@ZnO NR arrays/Apt. To assess the performance, the sensor was incubated with TOB solution of various concentrations at 37 °C for 1 h. After thoroughly rinsed with 10 mM PBS, the PEC response of the aptasensor towards TOB was recorded. The sequential electrodeposition preparation of a-MoS_x@ZnO core–shell NR arrays electrode for PEC aptasensing of TOB is schematically illustrated in Scheme 1.

3. Results and discussion

3.1. Material characterization

The morphological features of the ZnO NR arrays and a-MoS_x@ZnO NR arrays are investigated by field emission scanning electron microscope (FESEM) characterization. The typical SEM image of electrodeposited ZnO NR arrays is shown in Fig. 1A. From which, one can see that well aligned ZnO NRs uniformly cover the entire surface of ITO substrate. The small inset reveals that the nanorods exhibit regular hexagonal flat top surfaces with an average diameter of ca. 110 nm. After electrodeposition of a-MoS_x, a dense and uniform outer shell fully covers the surface of ZnO NR arrays (Fig. 1B). Especially, from the magnified SEM image of Fig. 1B, one can see clearly that the surface of ZnO NR becomes rougher and uneven, presenting many apophyses on the ZnO NR surfaces. The average thickness of a-MoS_x shell is ca. 17 nm, which can be adjusted by the deposition time. The core–shell nanostructure is further proved by transmission electron microscope

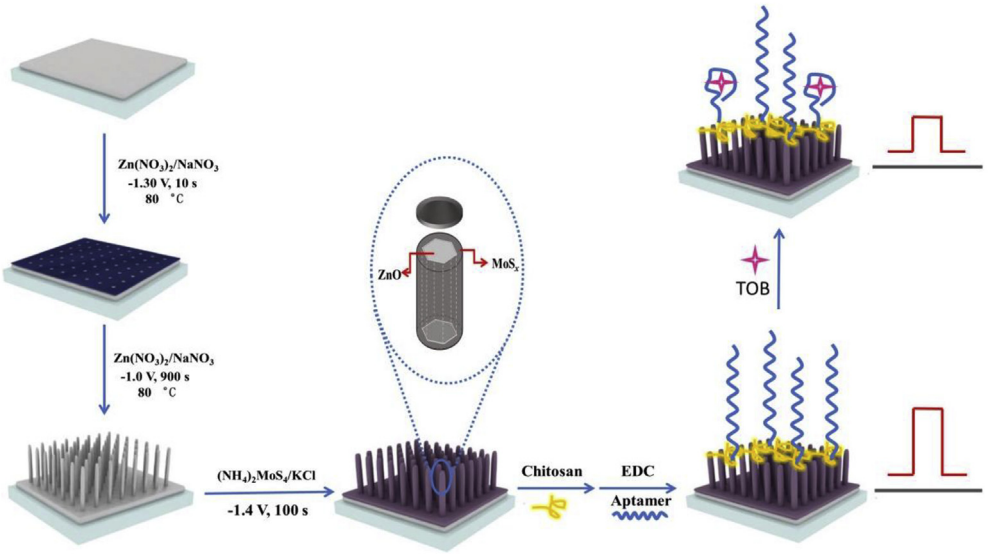

Scheme 1. Schematic illustration of the sequential electrodeposition preparation of a-MoS_x@ZnO core–shell NR arrays electrode for PEC aptasensing of TOB.

(TEM) study. In the TEM image of a-MoS_x@ZnO NR arrays (Fig. S2), the edges of nanorods become rough indicating that a-MoS_x film is uniformly deposited along the entire length of ZnO NR, and a tight interface between ZnO NR and a-MoS_x films might be formed during the sequential electrodeposition processes. As a result, the electron transfer from a-MoS_x to ZnO NR might be spatially smooth, which could be of benefit to enhancing the photocurrent response.

The crystal structure of the prepared material is studied by X-ray diffractometer (XRD). In the XRD pattern of ZnO NR arrays in Fig. 1C, the clear diffraction peaks at 31.8, 34.5, 36.3, and 62.9° can be indexed to the (100), (002), (101) and (103) lattice planes of wurtzite ZnO (PDF#36–1451), respectively. The predominant (002) peak manifests that the growth of ZnO NR on the ITO substrate is highly oriented in the (001) direction. For a-MoS_x@ZnO NR arrays, the major peaks of ZnO NR are still identifiable despite of notable decrease of the diffraction intensity. No diffraction peaks from MoS_x can be observed, indicating amorphous nature of the electrodeposited MoS_x film. This result is consistent with that in our previous reports (Shang et al. 2018a, 2018b).

Fig. 1D exhibits the comparable UV–visible absorption spectra of ZnO NR arrays, a-MoS_x@ZnO NR arrays and a-MoS_x film. As can be seen from the figure, oriented ZnO NR arrays displays a strong absorption below 400 nm, indicating a wide band gap of ZnO NR. After coating with the a-MoS_x shell, the visible absorption region of a-MoS_x@ZnO NR arrays is drastically broader, originating from the strong absorption of a-MoS_x film in a wide visible range. In addition, estimated from the band edge of UV–vis absorption, the band gap value of a-MoS_x (~685 nm) and ZnO nanorod (~428 nm) is ca. 1.81 eV and ca. 2.90 eV,

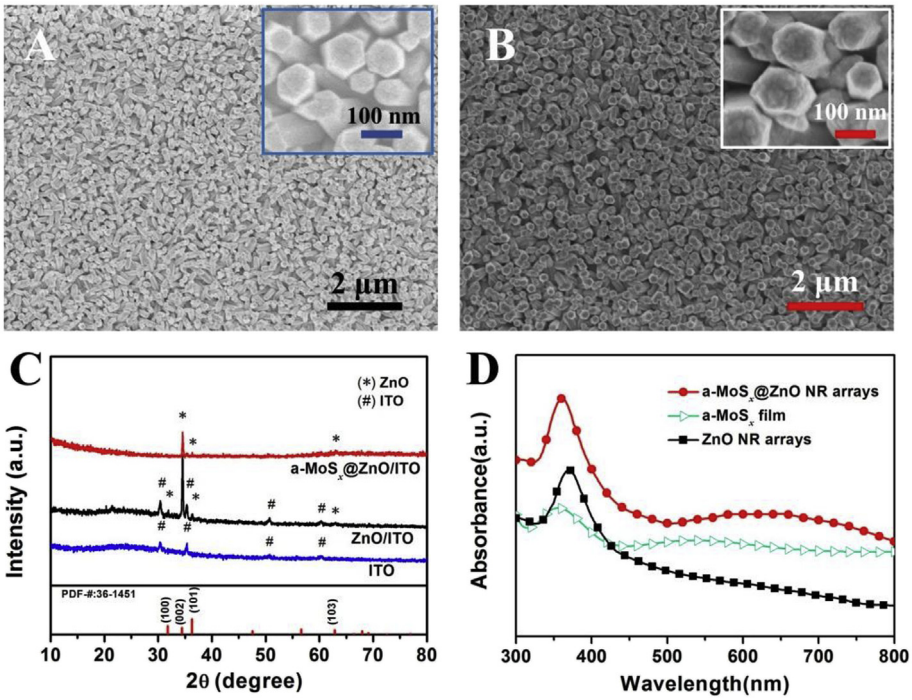

Fig. 1. FESEM images of (A) ZnO NR arrays and (B) a-MoS_x@ZnO NR arrays. (C) Comparative XRD patterns of a-MoS_x@ZnO NR arrays and ZnO NR arrays. (D) UV–visible absorption spectra of a-MoS_x@ZnO NR arrays, ZnO NR arrays and a-MoS_x film.

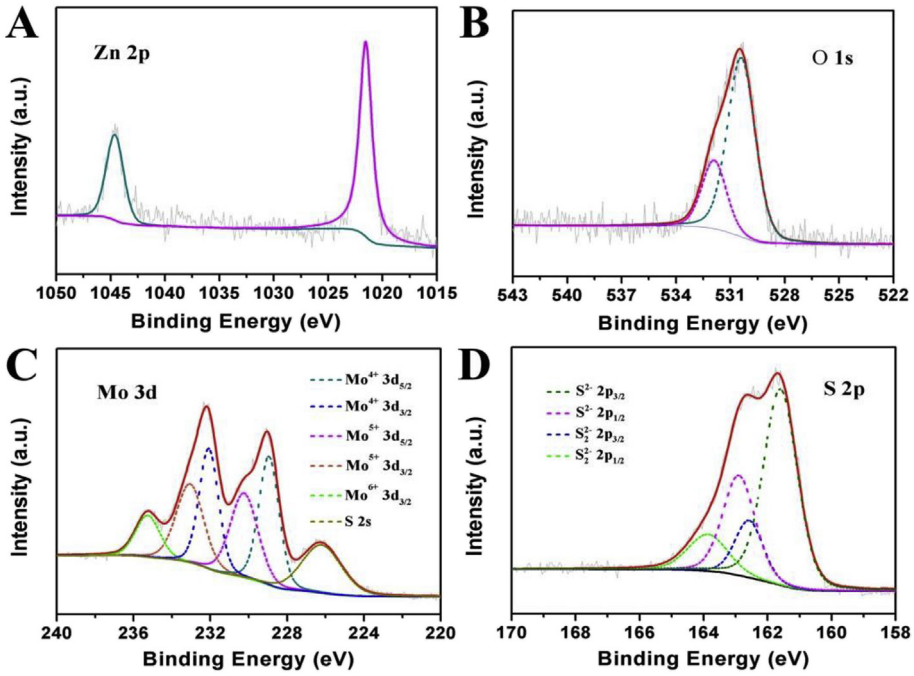

Fig. 2. High-resolution XPS spectra of (A) Zn 2p peaks, (B) O 1s peaks, (C) Mo 3d peaks and (D) S 2p peaks of a-MoS_x@ZnO NR arrays.

respectively. Thus, the sequentially electrodeposited core–shell a-MoS_x@ZnO NR arrays is able to efficiently utilize the visible spectrum, showing a promise in fabricating visible-light activated photoelectrode.

The chemical composition of the as-prepared material is further investigated by X-ray photoelectron spectroscopic (XPS). The high-resolution XPS spectra of Zn 2p, O 1s, Mo 3d and S 2p are shown in Fig. 2. The Zn 2p high resolution XPS spectrum (Fig. 2A) can be divided into two characteristic peaks at 1021.4 eV (Zn $2p_{3/2}$) and 1044.4 eV (Zn $2p_{1/2}$). The difference of the binding energy between the two peaks is 23.0 eV, confirming the formation of ZnO in the sample (Zhou et al., 2018). Furthermore, the asymmetric O 1s spectrum with two binding energy positions is exhibited in Fig. 2B. The peak at 530.4 eV corresponds to the lattice oxygen in the wurtzite structure of hexagonal ZnO. While the higher binding energy peak at 531.8 eV can be attributed to the chemisorbed oxygen on the surface and/or hydroxyls in the oxygen deficient regions within the ZnO matrix. It is reported that these species would be to the benefit of the separation of photogenerated electron-hole pairs during the photoelectrochemical processes (Mou et al., 2018; Wang et al., 2017). The Mo 3d spectrum in Fig. 2C can be fitted into five component peaks. The dominant peaks at 228.9 eV (Mo $3d_{5/2}$) and 232.1 eV (Mo $3d_{3/2}$) can be attributed to the Mo^{4+} of MoS_2. The doublet at 230.2 eV (Mo $3d_{5/2}$) and 232.9eV (Mo $3d_{3/2}$) indicates the existence of Mo^{5+}. The subpeak at 236.0 eV (Mo $3d_{3/2}$) is derived from Mo^{6+}. Besides, a peak at 226.1 eV is also observable, which corresponds to the characteristic binding energy of S 2s. In the S 2p spectrum shown in Fig. 2D, two distinct doublets are observed. The doublet at 161.7 eV (S $2p_{3/2}$) and 162.5 eV (S $2p_{1/2}$) is due to S^{2-} ions, as in the crystalline MoS_2 (Eda et al., 2011). The other doublet at higher binding energies at 163.0 eV (S $2p_{3/2}$) and 163.8 eV (S $2p_{1/2}$) might be derived from the bridging S_2^{2-} ligands and/or the apical S^{2-} ligand (Deng et al., 2016; Wan et al., 2017). In the electrodeposited MoS_x film, both Mo and S are multiple valence states, and the S/Mo ratio is ~2.1. These results indicate a complex composition and amorphous structure in nature.

3.2. Amplified visible-light PEC behavior of a-MoS_x@ZnO NR arrays

The PEC behaviors of oriented ZnO NR and a-MoS_x@ZnO NR arrays under visible light irradiation are compared in Fig. 3. The photocurrent–voltage (I–V) curves in Fig. 3A are tested from −0.2–1.0 V (vs. SCE) at a scan rate of 10 mV/s. Under the chopped visible illumination, both electrodes exhibit rapid photocurrent response and excellent switch behavior. Compared to the ZnO NR photoelectrode, the a-MoS_x@ZnO NR generates obviously enlarged photocurrent at any external potential. The transient photocurrent responses of these electrodes towards on/off cycles under visible illumination are studied at 0 V (vs. SCE). During each on/off cycle displayed in Fig. 3B, the photocurrent exhibits a short transient spike and then reaches immediately the steady state, which might be ascribed to the formation of a diffusion layer at the interface between the photoanode and electrolyte (Ding et al., 2018; Miao et al., 2013). The photoelectrochemical response of a-MoS_x@ZnO NR arrays is reproducible, and the photocurrent (778 nA) is ca. 3.4 times of that of ZnO NR arrays (229 nA). The improved PEC response could be mainly ascribed to the advantages of the sequential electrodeposited core/shell a-MoS_x@ZnO NR arrays electrode. Firstly, the vertically aligned ZnO NR arrays could provide a direct path for electron transport to the electrode surface, which considerably increases the separation efficiency of photoexcited electron–hole pairs. Secondly, the a-MoS_x film uniformly deposited on ZnO NR not only improves the visible-light absorption, but also enhances the photoelectrochemical conversion efficiency. Finally, as illustrated in Scheme 2, the well-matched band alignment between ZnO and a-MoS_x ensures the formation of a typical type II energy band structure (step-wise gap) in a-MoS_x@ZnO NR arrays. Under which configuration, the photoexcited holes and electrons can be efficiently separated and transferred while the hole-electron recombination process is simultaneously impeded, leading to enhanced photochemical response.

Since the thickness of a-MoS_x film could influence the photocurrent of a-MoS_x@ZnO NR arrays electrode, the deposition time-dependent film thickness of a-MoS_x was optimized. It could be observed from Fig. S3, the photocurrent increases with increasing deposition time of a-MoS_x film from 50 s to 100 s. The more a-MoS_x deposited, the higher visible light absorbed, and the more efficient electron-hole pairs separated. When the deposition time exceeds 100 s, excessive amount of a-MoS_x aggregated on the surface of ZnO NR arrays (Fig. S4), leading to a decrease in photocurrent. In subsequent study, deposition time of 100 s was therefore used to fabricate a-MoS_x film on the ZnO NR arrays.

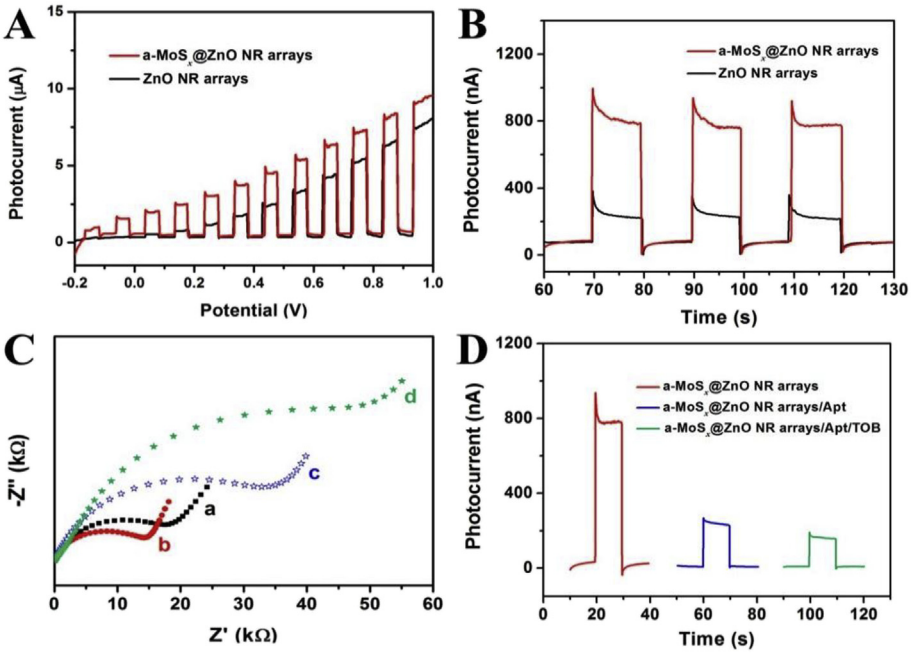

Fig. 3. (A) Photocurrent–voltage (*I–V*) curves of ZnO NR arrays and a-MoS$_x$@ZnO NR arrays under chopped visible illumination (scan rate: 10 mV/s). (B) Comparative photocurrent responses at 0 V towards on-off cycles under visible illumination. (C) Electrochemical impedance spectra of (a) ZnO NR arrays, (b) a-MoS$_x$@ZnO NR arrays, (c) a-MoS$_x$@ZnO NR arrays/Apt, and (d) a-MoS$_x$@ZnO NR arrays/Apt/TOB over the frequency range from 10 mHz to 100 KHz with amplitude of 5 mV in 0.1 M KCl containing 10 mM $K_3Fe(CN)_6/K_4Fe(CN)_6$. (D) Corresponding photocurrent responses of each electrode interface.

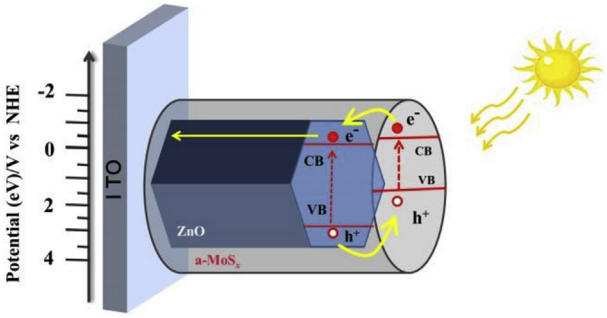

Scheme 2. Schematic illustration of the charge transport through the a-MoS$_x$@ZnO NR arrays electrode under illumination.

3.3. EIS and PEC investigations on the photoelectrode and aptasensing interface

Electrochemical impedance spectroscopic (EIS) measurement is performed to study the interfacial behavior of a-MoS$_x$@ZnO NR arrays electrode. The diameter of the semicircle in the impedance spectra in Fig. 3C reflects the interfacial electron-transfer resistance (R_{ct}). One can see that the diameter of a-MoS$_x$@ZnO NR arrays is smaller than that of the oriented ZnO NR, illustrating facilitated charge transport within the type II band structure of ZnO and a-MoS$_x$. Upon immobilizing TOB targeting aptamer on the photoelectrode surface, the R_{ct} increases dramatically due to inhibition of the electron transport from $[Fe(CN)_6]^{3-/4-}$ to the electrode by the aptamer blocking layer (Yan et al., 2015). When the aptasensing interface is incubated with TOB, the R_{ct} further increased originating from combination of the aptamer strands with the target molecules (Wang et al., 2018).

To monitor the construction processes of the proposed PEC aptasensor, the transient photocurrent response of each fabrication procedure was recorded at 0 V under visible light illumination. As illustrated in Fig. 3D, the a-MoS$_x$@ZnO NR arrays electrode exhibits a relatively high photocurrent of ca. 778 nA, attributed to enhanced visible light absorption and facilitated interfacial charge transport induced by decorating a-MoS$_x$ shell on the ZnO nanorod surface. Such high blank photocurrent could provide convenience for the proposed "single-off" PEC sensing for TOB. Subsequent incubation with the aptamer causes an obvious decrease of photocurrent (229 nA), due to suppressed interfacial electron transfer by the immobilized aptamer as indicated by EIS analysis. After the target TOB molecule is captured by the aptamer, the photocurrent is further depressed to 156 nA. This can be attributed to the increment in steric hindrance and the suppression of interfacial electron transfer by the possible conformational changes of the aptamer probe in the aptamer-analyte complex (Wang et al., 2018; Yan et al., 2015). Thus, the proposed ITO/a-MoS$_x$@ZnO NR arrays/Apt electrode can be utilized as the PEC sensor for quantitative determination of TOB.

3.4. Photoelectrochemical detection of TOB

Under optimal conditions (Fig. S5), the time-dependent current response of ITO/a-MoS$_x$@ZnO NR arrays/Apt electrode to TOB is investigated in 0.1 M PBS solution at 0 V under visible light illumination. Fig. 4A exhibits that the photocurrent gradually decreases with increasing TOB concentration. As displayed in Fig. 4B, the variation value of photocurrent linearly correlates to the logarithm of TOB concentration in the range of 0.010 ng/mL to 50 ng/mL. The linear regression equation is I_{Photo} (nA) = $-13.7 logC_{TOB}$ (ng/mL) + 168 (R^2 = 0.996). The detection limit is estimated to be 5.7 pg/mL (S/N = 3), which is lower than most of those in previous reports (summarized in Table S1).

3.5. Selectivity, stability and reproducibility

The selectivity of the proposed aptasensor is evaluated by analyzing the PEC response towards some antibiotics including tetracycline (TET), erythromycin (ERY), kanamycin (KAN) and chloramphenicol (CHL). As compared with TOB, all these antibiotics with 10-fold concentration do not cause obvious photocurrent change (Fig. 4C). The result reveals that the sensor possesses a satisfactory selectivity for TOB, origin from specific recognition between the aptamer and target molecule.

The stability and reproducibility of ITO/a-MoS$_x$@ZnO NR arrays/Apt electrode are also studied. Extremely stable photocurrent response under chopped light illumination for ten on/off cycles is obtained (Fig. 4D). Meanwhile, no noticeable change in the photocurrent is observed after the electrode was stored under 4 °C for 2 weeks, indicating a long-term storage stability. Employing six independently prepared ITO/a-MoS$_x$@ZnO NR arrays/Apt electrodes, the relative standard deviation (RSD) of photocurrent for 5 ng/mL TOB is 6.8% (Fig. S6),

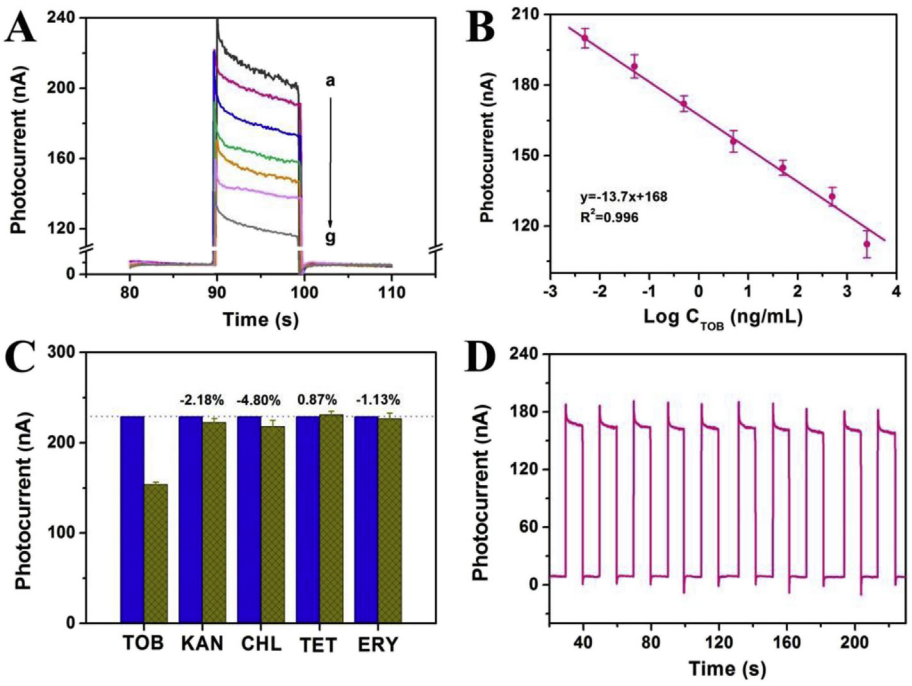

Fig. 4. (A) Photocurrent responses of a-MoS_x@ZnO NR arrays/Apt electrode to TOB with variable concentrations: (a) 0, (b) 0.010, (c) 0.050, (d) 0.50, (e) 5.0, (f) 10, (g) 50, (h) 100 ng/mL. (B) Corresponding calibration curve for TOB determination. The error bars are derived from the standard deviation of three measurements. (C) PEC responses toward TOB at 5 ng/mL and nontarget antibiotics at 50 ng/mL; (D) Stability test under chopped light illumination for ten on/off cycles. All the electrodes were evaluated at 0 V in 0.1 M PBS solution.

indicating acceptable reproducibility of the developed aptasensor.

3.6. Analysis of real samples

The applicability of the sensor in real samples is evaluated by the standard addition method. Different concentrations (0.06, 0.2, and 2 ng/mL) of standard TOB are spiked into human blood serum samples. As can be seen from Table S2, the average recovery of the aptasensor is in the range of 98.3–102.0% with RSD of 4.48–6.14%. The result demonstrates the reliability and potential applicability of the proposed aptasensor for TOB determination in real samples.

4. Conclusions

In summary, visible-light-activated a-MoS_x@ZnO NR arrays with high light switching stability has been successfully fabricated by facile all-electrodeposition for self-powered PEC aptasensing. The core-shell arrays electrode exhibits three-fold photocurrent compared to that of the ZnO NR arrays due to combination of a-MoS_x with favorable energy band alignment. By employing specific aptamer as recognition element, an ultrasensitive and selective PEC aptasensor for TOB determination at 0 V (vs. SCE) has been constructed. Rapid response in a wide linear range (0.010–50 ng/mL) with a low detection limit (5.7 pg/mL) was achieved. Desired accuracy and satisfactory recovery for trace tobramycin detection in serum samples was obtained, implying encouraging promise in practical applications. This work not only enriches the applications of a-MoS_x-based materials, but also provides a facile all-electrodeposition strategy for exploiting other low-cost and efficient hybrid structures for PEC biosensing as well as other photovoltaic installations.

Declaration of interest statement

The authors declare that they have no known competing financial interests or personal relationships that could have appeared to influence the work reported in this paper.

Conflicts of interest

There are no conflicts of interest.

CRediT authorship contribution statement

Mengxiang Shang: Conceptualization, Methodology, Investigation, Writing - original draft. **Jinling Zhang:** Writing - review & editing. **Hui Qi:** Resources, Data curation. **Yao Gao:** Investigation, Formal analysis. **Jianyue Yan:** Visualization, Data curation. **Wenbo Song:** Funding acquisition, Project administration.

Acknowledgment

This work was supported by the National Natural Science Foundation of China (No. 21874053 and No. 21475051), the Science and Technology Development Project of Jilin Province, China (No. 20180414022GH).

Appendix A. Supplementary data

Supplementary data to this article can be found online at https://doi.org/10.1016/j.bios.2019.04.019.

References

Arechederra, R.L., Minteer, S.D., 2011. Anal. Bioanal. Chem. 400 (6), 1605–1611.
Benck, J.D., Chen, Z.B., Kuritzky, L.Y., Forman, A.J., Jaramillo, T.F., 2012. ACS Catal. 2 (9), 1916–1923.
Bo, Y., Yang, H., Hu, Y., Yao, T., Huang, S., 2011. Electrochim. Acta 56 (6), 2676–2681.
Cappi, G., Spiga, F.M., Moncada, Y., Ferretti, A., Beyeler, M., Bianchessi, M., Decosterd, L., Buclin, T., Guiducci, C., 2015. Anal. Chem. 87 (10), 5278–5285.
Chen, Z.B., Forman, A.J., Jaramillo, T.F., 2013. J. Phys. Chem. C 117 (19), 9713–9722.
Deng, Y.L., Ting, L.R.L., Neo, P.H.L., Zhang, Y.J., Peterson, A.A., Yeo, B.S., 2016. ACS Catal. 6 (11), 7790–7798.
Devadoss, A., Sudhagar, P., Terashima, C., Nakata, K., Fujishima, A., 2015. J. Photoch. Photobio. C 24, 43–63.
Ding, X., Zhang, L., Wang, Y., Liu, A., Gao, Y., 2018. Coord. Chem. Rev. 357, 130–143.
Du, C.C., Huang, H., Feng, X., Wu, S.Y., Song, W.B., 2015. J. Mater. Chem. 3 (14), 7616–7622.
Dunne, P.W., Munn, A.S., Starkey, C.L., Lester, E.H., 2015. Chem. Commun. 51 (19), 4048–4050.
Eda, G., Yamaguchi, H., Voiry, D., Fujita, T., Chen, M.W., Chhowalla, M., 2011. Nano

Lett. 11 (12), 5111–5116.
Gong, Y.T., Wu, X.M., Dong, Y.M., Liu, Q.Y., Li, Z.J., Wang, G.L., 2018. Sensor. Actuator. B Chem. 266, 408–415.
Gonzalez-Fernandez, E., de-los-Santos-Alvarez, N., Lobo-Castanon, M.J., Miranda-Ordieres, A.J., Tunon-Blanco, P., 2011. Biosens. Bioelectron. 26 (5), 2354–2360.
Gonzalez-Fernandez, E., de-los-Santos-Alvarez, N., Miranda-Ordieres, A.J., Lobo-Castanon, M.J., 2013. Sensor. Actuator. B Chem. 182, 668–674.
Gu, T.T., Wu, X.M., Dong, Y.M., Wang, G.L., 2015. J. Electroanal. Chem. 759, 27–31.
Guo, M.X.M., Wrisley, L., Maygoo, E., 2006. Anal. Chim. Acta 571 (1), 12–16.
Gupta, V.K., Yola, M.L., Ozaltin, N., Atar, N., Ustundag, Z., Uzun, L., 2013. Electrochim. Acta 112, 37–43.
Han, X.Y., Zhang, Y.H., Nie, J.J., Zhao, S.Y., Tian, Y.P., Zhou, N.D., 2018. Microchim. Acta 185 (1). https://doi.org/10.1007/s00604-017-2568-6.
Huang, H., Feng, X., Du, C.C., Wu, S.Y., Song, W.B., 2015. J. Mater. Chem. 3 (31), 16050–16056.
Jiang, D., Du, X., Liu, Q., Hao, N., Wang, K., 2019. Biosens. Bioelectron. 126, 463–469.
Jin, D.Q., Xu, Q., Yu, L.Y., Hu, X.Y., 2015. Microchim. Acta 182 (11–12), 1885–1892.
Kang, Z., Yan, X.Q., Wang, Y.F., Zhao, Y.G., Bai, Z.M., Liu, Y.C., Zhao, K., Cao, S.Y., Zhang, Y., 2016. Nano Res 9 (2), 344–352.
Li, H., Shen, H., Duan, L.B., Liu, R.D., Li, Q., Zhang, Q., Zhao, X.R., 2018. Superlattice. Microst. 117, 336–341.
Liu, Q., Huan, J.A., Hao, N., Qian, J., Mao, H.P., Wang, K., 2017. ACS Appl. Mater. Interfaces 9 (21), 18369–18376.
Liu, S., Xing, X.R., Yu, J.H., Lian, W.J., Li, J., Cui, M., Huang, J.D., 2012. Biosens. Bioelectron. 36 (1), 186–191.
Liu, Z.Q., Zhang, X.M., Wang, B., Xia, M., Gao, S.Y., Liu, X.Y., Zavabeti, A., Ou, J.Z., Kalantar-Zadeh, K., Wang, Y.C., 2018. J. Phys. Chem. C 122 (24), 12589–12597.
Lu, H., Zhang, M., Guo, M., 2014. Appl. Surf. Sci. 317, 672–681.
Ma, Q., Wang, Y.X., Jia, J., Xiang, Y.H., 2018. Food Chem. 249, 98–103.
Miao, J.W., Yang, H.B., Khoo, S.Y., Liu, B., 2013. Nanoscale 5 (22), 11118–11124.
Morales-Guio, C.G., Hu, X.L., 2014. Acc. Chem. Res. 47 (8), 2671–2681.
Mou, H.Y., Song, C.X., Zhou, Y.H., Zhang, B., Wang, D.B., 2018. Appl. Catal. B Environ. 221, 565–573.
Peng, B., Tang, L., Zeng, G.M., Fang, S.Y., Ouyang, X.L., Long, B.Q., Zhou, Y.Y., Deng, Y.C., Liu, Y.N., Wang, J.J., 2018. Biosens. Bioelectron. 121, 19–26.
Rosasco, M.A., Bonafede, S.L., Faudone, S.N., Segall, A.I., 2018. J. Therm. Anal. Calorim. 134 (3), 1929–1941.
Shang, M.X., Du, C.C., Huang, H., Mao, J.X., Liu, P., Song, W.B., 2018a. J. Colloid Interface Sci. 532, 24–31.
Shang, M.X., Qi, H., Du, C.C., Huang, H., Wu, S.Y., Zhang, J.L., Song, W.B., 2018b. Sensor. Actuator. B Chem. 266, 71–79.
Tan, J., Yang, W., Oh, Y., Lee, H., Park, J., Moon, J., 2018. ACS Appl. Mater. Interfaces 10 (13), 10898–10908.
Tu, W.W., Wang, Z.Y., Dai, Z.H., 2018. Trac. Trends Anal. Chem. 105, 470–483.
Wan, X., Chen, K., Chen, Z.F., Xie, F.Y., Zeng, X.L., Xie, W.G., Chen, J., Xu, J.B., 2017. Adv. Funct. Mater. 27 (19). https://doi.org/10.1002/adfm.201603998.
Wang, J., Xia, Y., Zhao, H.Y., Wang, G.F., Xiang, L., Xu, J.L., Komarneni, S., 2017. Appl. Catal. B Environ. 206, 406–416.
Wang, M.H., Hu, B., Yang, C., Zhang, Z.H., He, L.H., Fang, S.M., Qu, X.W., Zhang, Q.X., 2018. Biosens. Bioelectron. 99, 176–185.
Wu, S.Y., Huang, H., Shang, M.X., Du, C.C., Wu, Y., Song, W.B., 2017. Biosens. Bioelectron. 92, 646–653.
Yan, K., Liu, Y., Yang, Y.H., Zhang, J.D., 2015. Anal. Chem. 87 (24), 12215–12220.
Yang, R.Y., Yan, X.X., Li, Y.M., Zhang, X.H., Chen, J.H., 2017. ACS Appl. Mater. Interfaces 9 (49), 42482–42491.
Yang, Y., Cheng, Y.F., 2018. Electrochim. Acta 276, 311–318.
Zang, Y., Fan, J., Ju, Y., Xue, H.G., Pang, H., 2018. Chem. Eur J. 24 (53), 14010–14027.
Zhao, W.W., Xu, J.J., Chen, H.Y., 2016. Trac. Trends Anal. Chem. 82, 307–315.
Zhou, Y., Gao, C., Guo, Y.C., 2018. J. Mater. Chem. 6 (22), 10286–10296.